Three-Dimensional Hypersonic Nonequilibrium Flows at Large Angles of Attack

Bilal A. Bhutta* and Clark H. Lewis†
VRA, Inc., Blacksburg, Virginia

A new three-dimensional nonequilibrium (PNS) scheme is developed to study the effects of large angles of attack on the hypersonic flowfield and the species concentration dstributions around a typical sphere-cone reentry vehicle. A new predictor-corrector solution scheme is developed along with a new fully implicit and crossflow coupled shock-fitting scheme to predict the bow shock location as a part of the marching solution under large-angle-of-attack conditions. The Mach 20 flowfield around a 7 deg sphere-cone at a flight altitude of 175 kft is studied under 20 deg angle-of-attack conditions. The results clearly show the accuracy, efficiency, and grid-refinement capabilities of the new three-dimensional nonequilibrium PNS scheme.

Nomenclature

CA = axial-force coefficient
CFW = crossflow skin-friction coefficient
C_i = mass fraction of ith species
CM = pitching-moment coefficient
CN = normal-force coefficient
C_p = specific heat at constant pressure
D_i = binary diffusion coefficient for the ith species
h = static enthalpy of the mixture
h_i = static enthalpy of the ith species
J = determinant of the transformation Jacobian
J_i = x, y, and z component of the mass-flux of the ith species, $\epsilon_1 C_i$, x_i
k = thermal conductivity
L = body length
Le = Lewis number, $\rho \bar{C}_p D_i / \bar{k}$
M = Mach number
m = molecular weight
m_{njk} = $\xi_{n,x_j} \xi_{n,x_k}$
NS = total number of chemical species
P,p = static pressure
PHI = circumferential angle ϕ
Pr = Prandtl number
QW = total wall heat-transfer rate
R = radial distance from the body axis
R_b = local body radius
Re = Reynold number, $(\rho VRn)/\mu$
RN,Rn = nose radius
$RSHK$ = radial location of the bow shock
T = static temperature
U_j = contravariant velocities $u_k \xi_{j,x_k}$
u = x-component of mass-averaged velocity
u^* = friction velocity, $(\tau/\rho)^{0.5}$
u_j = u, v, and w for $j = 1,2$ and 3
V = total mass-averaged velocity
v = y-component of mass-averaged velocity
w = z-component of mass-averaged velocity
X,x = coordinate along body axis
x_j = x,y, and z for $j = 1,2$, and 3
y^+ = $\rho(R - R_b)u^*/\mu$
XCP = axial location of the center of pressure
α = angle of attack
ϵ = M_∞ / Re_∞
ϵ_1 = $\epsilon Le/\rho$
ϕ = circumferential angle measured from the windward side
$\dot{\omega}i$ = production rate of the ith species
ξ_1 = marching or streamwise coordinate
ξ_2 = coordinate measured from the body to the outer bow shock
ξ_3 = coordinate measured from the windward to the leeward direction
ρ = mixture density
ρ_i = density of the ith species
τ = shear stress
χ = intermediate solution vector after the corrector step
χ^* = intermediate solution vector after the predictor step
Σ = summation over all species, $i = 1,2,3,\ldots,NS$

Superscripts

n = index for iteration
j = index in ξ_1 direction
$-$ = mixture property

Subscripts

$,$ = represents partial derivative
∞ = freestream quantity
w = wall quantity
i = represents ith chemical species
j,k,l = indicial notation representing 1, 2, and 3

Received May 13, 1988; presented as Paper 88-2568 at the AIAA 6th Applied Aerodynamics Conference, Wiliamsburg, VA, June 6-8, 1988; revision received Nov. 10, 1988.

*Chief Scientist. Member AIAA.
†President. Associate Fellow AIAA.

Introduction

OVER the past few years the development of accurate prediction schemes for three-dimensional, finite-rate, chemically reacting flowfields around realistic re-entry configurations has become the focus of much attention. Until recently the available numerical schemes for predicting finite-rate, chemically reacting, viscous external flows have been restricted to either boundary-layer type methods (e.g., Blottner et al.[2]) or viscous shock-layer (VSL) schemes (Miner and Lewis,[3] Kim et al.,[4] and Swaminathan et al.[5]). High-altitude hypersonic re-entry flows are, in general, characterized by low Reynolds numbers. Because of such typically low Reynolds number flows, the application of boundary-layer methods has encountered significant difficulties (such as displacement-thickness interaction, streamline tracking, determination of edge conditions, etc.). The VSL methods, on the other hand,

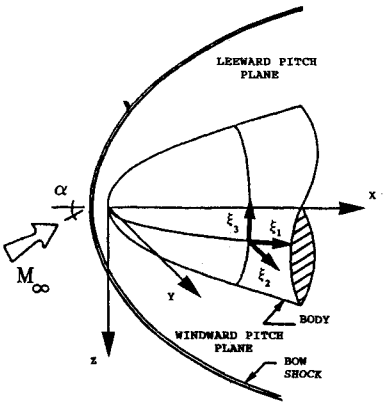

Fig. 1 Cartesian and general curvilinear coordinate system.

have been shown to have great potential for analyzing such nonequilibrium viscous re-entry flows, especially in the blunt-body region. The three-dimensional VSL schemes are, however, parabolic in the crossflow direction and, thus, cannot treat the large crossflow separated regions that occur under high angle-of-attack conditions. Short of a three-dimensional nonequilibrium Navier-Stokes solution, the parabolized Navier-Stokes (PNS) schemes represent the most promising methods for a detailed and accurate analysis of the leeward flowfield and flowfield chemistry.

In our earlier studies we have successfully developed and used a new fully interative PNS solution scheme for three-dimensional, finite-rate, chemically reacting Earth re-entry flows. Our previous studies with this three-dimensional nonequilibrium PNS scheme have been very encouraging (Bhutta and Lewis,[6-9] and Bhutta et al.[10]). However, the application of this scheme was limited to only small-to-moderate (<5 deg) angle-of-attack conditions. In this paper we have extended our earlier nonequilibrium PNS scheme to study the effects of large angles of attack on the flowfield and the species concentration distributions around a typical sphere-cone re-entry vehicle under hypersonic flight conditions. Substantial extensions, modifications, and developments were done to be able to adequately address this large angle-of-attack problem and its associated numerical complications. To account for the strong crossflow coupling effects that exist in the regions of crossflow separation, a new predictor-corrector solution scheme has been developed along with a full implicit and cross-flow coupled shock-fitting scheme to predict the bow shock location as a part of the marching solution. Three different grids were used to study the flow around a 7 deg sphere-cone at Mach 20 under 20 deg angle-of-attack conditions. The results will clearly show the accuracy, efficiency, and grid-refinement capabilities of the current three-dimensional nonequilibrium PNS scheme.

Solution Scheme

The coordinate system used for the current three-dimensional PNS scheme is a general curvilinear coordinate system (ξ_1,ξ_2,ξ_3) shown in Fig. 1. Also, a body-fixed orthogonal (Cartesian) coordinate system is chosen such that the origin of the Cartesian coordinate system is at the tip of the blunt nose, and the x axis is aligned with the axis of the body. The z axis is chosen as pointing downward such that the windward surface of the vehicle is on the positive z-axis side. The ξ_1 coordinate is along the body and is also the marching direction. The ξ_2 coordinate stretches from the body to the outer bow shock and lies in an axis-normal plane. The ξ_3 coordinate is measured in the crossflow direction from the windward pitch plane. In general, it is assumed that the (x,y,z) space is uniquely transformable to the (ξ_1, ξ_2, ξ_3,) space such that, at each marching step, every grid cell in the x, y, z space is transformed into a unit cube.

In our approach we choose the flowfield unknowns to be the density ρ, the density-velocity products ρu, ρv, and ρw, the density-temperature product ρT, and the pressure p. Thus our vector of unknowns is

$$q = [\rho,\ \rho u,\ \rho v,\ \rho w,\ \rho T,\ p]^T \tag{1}$$

Following the approach of Peyret and Viviand[11] and Viviand[12] it can be shown that the full Navier-Stokes equations governing the nonequilibrium flow problem (Bird et al.[13]) can be nondimensionalized and transformed into the general curvilinear coordinate system (ξ_j); i.e.,

$$(f_j - \epsilon s_j)_{,\xi_j} = h \tag{2a}$$

These five equations representing the differential conservation of mass, momentum, and energy are mathematically closed by using the equation of state for the particular gas model being used. This equation of state can be written in a general functional form as

$$f(\rho,T,p,C_i) = \bar{m}p - \rho T = 0 \tag{2b}$$

These equations are elliptic in ξ_1, ξ_2, and ξ_3 directions. If we neglect the diffusion and dissipation effects in the ξ_1 direction and assume a constant Lewis number, we can simplify Eqs. (2a) and (2b) and write the final parabolized Navies-Stokes equations in the following vectorial form

$$f_{j,\xi_j} - \epsilon(s_{2,\xi_2} + s_{3,\xi_3}) = h \tag{3a}$$

The various components of this vectorial equation are defined as

$$f_j = (1/J)\begin{bmatrix} \rho U_j \\ \rho u U_j + \xi_{j,x}p \\ \rho v U_j + \xi_{j,y}p \\ \rho w U_j + \xi_{j,z}p \\ (\bar{C}_pT + 0.5V^2)\rho U_j \\ 0 \end{bmatrix} \tag{3b}$$

$$s_n = (\bar{\mu}/J)\begin{bmatrix} 0 \\ m_{nkk}u_{,\xi_n} + (m_{n1j}u_j,_{\xi_n})/3 \\ m_{nkk}v_{,\xi_n} + (m_{n2j}u_j,_{\xi_n})/3 \\ m_{nkk}w_{,\xi_n} + (m_{n3j}u_{j,\xi_n})/3 \\ m_{nkk}T_{,\xi_n}\bar{C}_p/Pr + m_{nkk}u_ju_{j,\xi_n} + m_{njk}u_ju_{k,\xi_n}/3 \\ 0 \end{bmatrix} \tag{3c}$$

where no summation is implied over n, which takes the values of $n=2$ and $n=3$, respectively, and

$$h = \begin{bmatrix} 0 \\ 0 \\ 0 \\ 0 \\ \left\{\sum\left[\dfrac{\epsilon_1 m_{2kk}\bar{\mu}}{Pr}T_{,\xi_2}(c_p)_iC_{i,\xi_2} - h_i\dot{\omega}_i\right] + \rho TU_j\bar{C}_{p,\xi_j}\right\}/J \\ \bar{m}p - \rho T \end{bmatrix} \tag{3d}$$

The species concentrations C_i are obtained from the three-dimensional, species-conservation equations. It should be noted that in the conservation equations of mass, momentum, and energy we did not neglect the crossflow viscous effects. However, in order to further simply the species conservation equations we neglect the crossflow as well as streamwise diffu-

sion terms appearing in these species conservation equations. The final thin-layer parabolized species conservation equations are written as

$$U_j C_{i,\xi_j} + \epsilon_1[\xi_{2,x_j}(\bar{\mu}\xi_{2,x_j}/Pr)_{,\xi_2}]C_{i,\xi_2} + \epsilon_1[\bar{\mu}m_{2kk}/Pr]C_{i,\xi_2\xi_2} = \dot{\omega}_i/\rho \quad (4)$$

where $i = 1,2,3,\ldots,(NS-1)$.

The overall nonequilibrium PNS problem represented by Eqs. (3) and (4) is well-posed. However, the number of unknowns involved in very large (i.e., ρ, ρu, ρv, ρw, ρT, p, $\overline{C_p}$, $\overline{k}$, $\overline{m}$, $\bar{\mu}$, Pr, C_1, C_2, $C_3,\ldots,C_{NS}$). However, for many practical problems, the coupling between the fluid mechanics (ρ, ρu, ρw, ρT, and p) and the chemistry ($\overline{C_p}$, $\overline{m}$, $\overline{k}$, $\bar{\mu}$, Pr, C_1, $C_2,\ldots,C_{NS}$) is not very strong. With this idea in mind, we can decouple the overall nonequilibrium PNS problem into 1) a fluid mechanics problem and 2) a chemistry problem. The coupling between the fluid mechanics and the chemistry is taken care of in an iterative manner.

Fluid-Mechanics Problem

If we assume that the solution at the $n+1$ level is close to the solution at the nth iteration, we can use a first-order Taylor series expansion around the previous iteration. Although the grid also changes from one iteration to the next, it is assumed that these changes are small and do not contribute to the Jacobian matrices. Now, as can be seen from Eqs. (3), the governing flowfield equations are elliptic in the ξ_2 and ξ_3 directions so that for second-order accuracy we use central-differenced approximations for all ξ_2 and ξ_3 derivatives. However, the use of central-differenced schemes is typically associated with solution oscillations (Kaul and Chaussee,[14] Bhutta and Lewis,[6-9] Schiff and Steger,[15] and Shank et al.[16]). This oscillatory behavior becomes more pronounced if the local velocities are small, so that the diagonal terms of the Jacobian matrices become relatively small also. In order to damp these solution oscillations, it is necessary to add some additional higher-order diffusion terms to Eqs. (3). In our earlier work (Bhutta and Lewis[6-9] and Bhutta et al.[10]), we developed a second-order, fully implicit smoothing approach that is accurate and simple to use. In the present study we extend this basic approach such that (to second-order accuracy) we can rewrite Eqs. (3) in terms of an intermediate solution χ as

$$[f_j(\chi)]_{,\xi_j} - \epsilon[s_2(\chi)]_{,\xi_2} - \epsilon[s_3(\chi)]_{,\xi_3} - h(\chi) = (A_1/\Delta\xi_1 - A_0)\cdot\chi_{,\xi_3\xi_3}\Delta\xi_3^2/4 = \pi\Delta\xi_3^2 \quad (5a)$$

where

$$q^{j+1} = \chi + \chi_{,\xi_2\xi_2}\Delta\xi_2^2/4 \quad (5b)$$

The right-hand side of Eq. (5a) gives the appropriate form of the implicit and explicit crossflow smoothing operator to be added to the implicit (left-hand) side and the explicit (right-hand) side of Eq. (5a). As far as the smoothing effects in the ξ_2 direction are concerned [Eq. (5b)], they are further modified to limit them to only the pressure field. In this manner the velocity and temperature gradients near the wall remain unaffected and, consequently, there is no degradation of the wall heat-transfer and skin-friction predictions.

Thus the final form of the system of equations to be solved becomes

$$(A_1/\Delta\xi_1 - A_0)^n\cdot(\Delta\chi - \Delta\chi_{,\xi_3\xi_3}\Delta\xi_3^2/4)^{n+1} + [(A_2 - \epsilon M_2)^n\cdot\Delta\chi^{n+1}]_{,\xi_2} + [(A_3 - \epsilon M_3)^n\cdot\Delta\chi^{n+1}]_{,\xi_3} = -[f_{j,\xi_j} - \epsilon(s_{2,\xi_2} + s_{3,\xi_3}) - h]^{j+1,n} + \pi\Delta\xi_3^2 = g^{j+1,n}$$

where

$$q^{j+1} = \chi + [0,0,0,0,0,(p_{,\xi_2\xi_2}\Delta\xi_2^2/4)]^T$$

Chemistry Problem

For the chemistry problem, we use a seven-species (O, O_2, N, N_2, NO, NO^+, and e^-) gas model to represent the finite-rate chemically reacting air mixture. The thermodynamic properties of these species are obtained from the thermodynamic data of Browne.[17-19] The diffusion model used in this seven-species model is limited to binary diffusion, with the binary diffusion coefficient for each gas species defined by a Lewis number of 1.4.

The gas-phase reactions considered in this seven-species air system correspond to the model used by Blottner et al.[2] and Miner and Lewis,[3] and use the reaction-rate data proposed by Bortner.[20] The viscosities of O, O_2, N, N_2, NO, NO^+, and e^- are computed from the curve-fit relations used by Blottner et al.,[2] and the thermal conductivities of these species are estimated with the Eucken semi-empirical formula. After the viscosities and thermal conductivities of the individual species have been estimated, the viscosity and thermal conductivity of the mixture are calculated using Wilke's semi-empiricial relations.

In our current solution approach the species conservation equations are solved in an uncoupled manner. In treating the species conservation equations in such a way, special consideration needs to be given to the treatment of the species production terms. It is known that a full linearization of these production terms results in an unstable solution under typical flight conditions. For this reason it is necessary to split the overall production term into two parts (Blottner et al.[2] and Miner and Lewis[3]).

$$(\dot{\omega}_i/\rho) = \dot{\omega}_i^0 - \dot{\omega}_i^1 C_i \quad (6)$$

The calculations of these production terms involve several exponential and logarithmic operations to be performed for each species. For a typical nonequilibrium-air system there are several species involved and, consequently, a substantial part of the total computing time can easily be spent in doing these calculations. In our current three-dimensional nonequilibrium PNS scheme we have taken a new approach of a partial streamwise linearization of these production terms. In our approach, as in Eq. (6), the production terms are still separated into an explicit contribution ($\dot{\omega}_i^0$) and an implicit contribution ($\dot{\omega}_i^1$). However, these components are linearized based on the flowfield and chemistry information from the previous marching step and, thus, need to be calculated only once at each marching step. Since this linearization in only partial and is done on quantities that indeed change very slowly (especially in the PNS afterbody region), the errors introduced are very small. However, the computing-time efficiency achieved is substantial.

Initial and Boundary Conditions

The problem represented by the governing PNS equations is a split-boundary-value problem and requires initial conditions as well as boundary conditions at the wall, at the outer bow shock, and in the pitch-plane of symmetry. The initial conditions to start the nonequilibrium PNS solutions were obtained from a nonequilibrium VSL blunt-body solution scheme. The quality of such VSL solutions has been discussed in great detail by Bhutta and Lewis,[6-9] Bhutta et al.,[21] Thompson et al.[22] and Swaminathan et al.[5] The VSL blunt-body solution is interpolated to obtain the starting solution at the initial data plane (IDP) for the three-dimensional PNS afterbody solution. We typically generate the IDP at the most upstream nose-afterbody tangent point location.

For the fluid mechanics problem of the nonequilibrium PNS equations, the boundary conditions at the wall consist of six independent relations representing the nature of the gas mixture and the physical conditions at the wall. These conditions are 1) the equation of state of the gas, 2-4) no slip conditions for the three velocity components, 5) the specified wall temperature condition and 6) the condition of zero pressure derivative

in the ξ_2 direction. The boundary condition on the pressure derivative comes from a boundary-layer-type analysis performed at the wall. These six boundary conditions are well-posed and from a linearly independent set. For the chemistry problem of the aforementioned nonequilibrium PNS solution scheme represented by the species conservation equations [Eq. (4)], the wall boundary conditions used consist of either 1) a fully-catalytic wall [$C_i = C_{i\infty}$], or 2) a non-catalytic wall [$C_{i,\xi_2} = 0$]. In the current study, however, we have only used fully-catalytic wall boundary conditions.

The boundary conditions at the outer bow shock involve a fully implicit and crossflow coupled shock-fitting approach, and the bow shock is predicted at the solution marches down the body. The windward and leeward pitch planes consist of reflective or symmetric boundary conditions. The symmetric and reflective boundary conditions used in the present study are based on the second-order crossflow boundary conditions used by Kaul and Chaussee[14] and Shanks et al.[16]

Predictor-Corrector Solution Scheme

It should be noted that the right-hand side of Eq. (5a) is the governing differential equation corresponding to the fluid mechanics problem written at the nth iteration level and goes to zero in the limit of convergence. As discussed by Bhutta and Lewis,[6-9] under these conditions the exact from of the left-hand implicit terms is of no great consequence except that it affects the convergence path of the solution. With this idea in mind we do not update the Jacobian matrices beyond the first iteration. Under large-angle-of-attack conditions, strong crossflow separated regions may develop on the leeward side. Under these conditions, solution coupling in the crossflow direction is very important. If these coupling effects are not properly considered during the iterative solution, they can cause severe convergence difficulties. In order to address that problem of crossflow coupling we have developed a new predictor-corrector approach. This predictor-corrector scheme is divided into three different parts; namely, 1) the predictor solution, 2) the shock solution, and 3) the correct solution.

The overall block-pentadiagonal system of equations to be solved can be written as

$$[\boldsymbol{A}\cdot\Delta\chi_{k,\ell-1}] + [\boldsymbol{B}\cdot\Delta\chi_{k,\ell}] + [\boldsymbol{C}\cdot\Delta\chi_{k,\ell+1}] + [\boldsymbol{D}\cdot\Delta\chi_{k-1,\ell}] + [\boldsymbol{E}\cdot\Delta\chi_{k+1,\ell}] = -[\boldsymbol{f}_{j,\xi_j} - \epsilon\boldsymbol{s}_{2,\xi_2} - \epsilon\boldsymbol{s}_{3,\xi_3} - \boldsymbol{h}]^{j+1,n} + \pi\Delta\xi_3^2 = \boldsymbol{g}^{j+1,n} \tag{7}$$

Predictor Solution

In the predictor step we neglect the implicit crossflow (ξ_3) coupling effects in Eq. (7) in favor of the axis-normal (ξ_2) coupling effects. With this assumption the equations for the predictor step take the following block-tridiagonal form

$$[\boldsymbol{A}\cdot\Delta\chi^*_{k,\ell-1}] + [\boldsymbol{B}\cdot\Delta\chi^*_{k,\ell}] + [\boldsymbol{C}\cdot\Delta\chi^*_{k,\ell+1}] = \boldsymbol{g}^n \tag{8a}$$

These equations are inverted from the body ($\ell = 1$) to the shock ($\ell = LMAX$) to develop recursive relations between the solution at each successive grid point in the ξ_2 direcion. These recursive relations have the form

$$\Delta\chi^*_{k,\ell} = -\boldsymbol{R}_{k,\ell}\cdot\Delta\chi^*_{k,\ell+1} + \boldsymbol{r}^n_{k,\ell} \tag{8b}$$

where $k = 1,\ldots,KMAX$ and $\ell = 1,\ldots,LMAX-1$.

Crossflow-Coupled Fully Implicit Shock Solution

We have also developed a new fully implicit and crossflow-coupled shock-fitting scheme that correctly predicts the bow shock shape as a part of the marching solution. This scheme is fully iterative and can accurately treat various gas models in a unified manner. Unlike earlier noniterative shock-propagation approaches (Chaussee et al.,[23] Shanks et al.,[16] and Kaul and Chaussee[14]), the current approach does not assume the flowfield behind the shock to be inviscid and does not neglect the crossflow coupling effects at the shock. This can be especially important when dealing with complex three-dimensional configurations where the three-dimensional nature of the body can interact with the bow shock and substantially distort it. Similar strong crossflow variations may also occur on simple configurations when pitched at large angles of attack. Furthermore, unlike the iterative shock-fitting approaches of Helliwell et al.[24] and Lubard and Helliwell,[25] the current shock-fitting approach does not increase the size of the matrix solution between the body and the shock.

In developing the present bow shock-fitting scheme, we assume that from one iteration to the next the shock-points move along the ξ_2 grid line. This assumption allows us to reduce the number of unknowns to be solved, and the final solution has only one additional unknown at the shock that completely defines the spatial movement of the shock point. This smaller number of unknowns is very important for faster iterative solution and faster convergence characteristics of the overall implicit shock-prediction scheme. Denoting the amount by which the shock point moves in the ξ_2 direction as Δ_s, the corresponding movement of the shock-point coordinates from one iteration to the next can be written as

$$(x_j)^{n+1}_s \simeq (x_j)^n_s + (x_{j,\xi_2})^n_s(\Delta)^{n+1}_s \tag{9}$$

Consequently, we can define three orthogonal shock-normal and shock-tangent directions at the shock surface in terms of the shock coordinates and, thus, the shock movement (Δ_s).

Having defined the relevant velocity components for the purpose of writing the five Rankine-Hugoniot (frozen) shock-crossing equations (representing the conservation of mass, momentum, and energy), we note that we have actually seven unknowns at the shock. These seven unknowns are written in a vectorial form as

$$\boldsymbol{q}_s = [\rho,\rho u,\rho v,\rho w,\rho T,p,\Delta]^T_s \tag{10}$$

Thus, we need two more equations to close the system of equations at the shock. One of these additional equations is the equations is the equation of state and gas, and the other equation is provided by applying the differential continuity of mass equation behind the shock. As we can see, no approximation other than the assumption of a frozen Rankine-Hugoniot shock has been made. These equations are equally valid whether the conditions behind the shock are viscous or inviscid dominated or whether substantial flowfield gradients exist behind the shock.

The use of the differential continuity equation behind the shock provides the implicit coupling between the flowfield behind the shock ($\ell = LMAX$) and the flowfield at the grid point adjacent to it ($\ell = LMAX-1$). Using the recursive relations of the predictor step at $\ell = LMAX-1$ [see Eq. (8b)], the shock equations can be reduced to a block-tridiagonal system of equations in the crossflow direction. These equations are then solved using appropriate boundary conditions in the leeward and windward pitch planes of symmetry. This solution gives simultaneously the $\Delta\boldsymbol{q}^{n+1}_s$ vectors at each shock point ($k = 1,\ldots,KMAX$). Using this shock-point solution as the predictor solution at the shock along with the recursive relations of Eq. (8b), we can now obtain the predictor solution (χ^*) for all interior grid points ($\ell = 1,\ldots,LMAX-1$). Furthermore, the new x,y, and z coordinates of the shock point locations are now determined using Eq. (10).

Corrector Solution

Just like the shock-point solution, the solution in the corrector step uses the recursive relations from the predictor step to eliminate the $(k,\ell-1)$ contributions in the original block-pentadiagonal system [(Eq. (7)]. If we further assume that the solution at the $(k,\ell+1)$ point can be approximated from the

predictor step, one can reduce the Eq. (7) to only a coupled block-tridiagonal system in the crossflow direction. The equations for the corrector step can now be written as

$$D \cdot \Delta\chi_{k-1,\ell} + (B - AR_{k,\ell-1}) \cdot \Delta\chi_{k,\ell} + E \cdot \Delta\chi_{k+1,\ell} \cong (g^n - A \cdot r^n_{k,\ell-1}) - C \cdot \Delta\chi^*_{k,\ell+1} \quad (11)$$

or simply

$$D \cdot \Delta\chi_{k-1,\ell} + (B - AR_{k,\ell-1}) \cdot \Delta\chi_{k,\ell} + E \cdot \Delta\chi_{k+1,\ell} = (B - AR_{k,\ell-1}) \cdot \Delta\chi^*_{k,\ell} \quad (12)$$

This system of block-tridiagonal equations is now solved using plane-of-symmetry boundary conditions applied in the windward and leeward pitch planes. In this way the corrected flowfield solution (χ) is obtained within the shock layer. Once the flowfield solution as well as the shock shape converges, the final smoothed solution (q^{j+1}) is then obtained using Eq. (5b).

Results and Discussion

In order to demonstrate the three-dimensional nonequilibrium PNS capability developed in this study, we studied the flow around a sphere-cone configuration under large-angle-of-attack hypersonic flight conditions. The sphere-cone configuration considered consists of a 7 deg forecone with a 2 in. nose radius and an overall length of 20 in. The freestream conditions for this test case are given in Table 1, and consist of a flight altitude of 175 kft, a flight Mach number of 20, and an angle of attack of 20 deg. The wall temperature was assumed to be 2000°R, and the vehicle surface was assumed to be fully catalytic.

Three different grids were used to study this test case and evaluate the accuracy, efficiency, and grid-refinement capabilities of our three-dimensional PNS scheme. Case 1 consists of 31 crossflow planes and 30 points between the body and the shock. Case 2 consist of 31 crossflow planes and 50 points between the body and the shock, while case 3 consists of 51 crossflow planes and 30 points between the body and the shock. In each case a cylindrical grid generation scheme was used with the crossflow planes located at equal angular increments. The grid point distribution between the body and the shock consists of an exponential distribution near the wall and an equally spaced grid away from the wall. For cases 1 and 2 at the body and the y^+ values at the wall are between 0.8 and 1.0 whereas for case 3 the corresponding y^+ values are between 0.4 and 0.5.

In order to check the accuracy of the current three-dimensional nonequilibrium PNS scheme, we compared these predictions with the corresponding predictions of our viscous shock-layer (VSL) scheme.[5] The inviscid NOL3D code[26] was also used to compare the prediction of surface pressure, shock shape, and the vehicle force and moment data. Before evaluating these results there are a few points that need to be kept in mind. Both the VSL and NOL3D results are for a crude grid using only 9 circumferential planes, whereas the PNS results shown are for 51 crossflow planes (case 3). Furthermore, it should be noted that the VSL solution cannot treat the crossflow separated region, and the VSL predictions very close to the point of crossflow separation may not be very accurate. The results show that for the test case considered, the VSL solution predicts crossflow separation occurring between an axial location of 2–3 nose radii, while the PNS solution predicts the crossflow separation occuring between axial location of 3–4 nose radii.

Table 1 Freestream conditions for the test cases

Quantity	
Mach number	20.000
Reynolds number	1.34E+4
Pressure, lbs/ft^2	1.102
Density, slug/ft^3	1.32E−6
Temperature, R	485.151
Velocity, ft/s	2.16E+4
Angle of attack, deg	20.000
Wall temperature, R	2000.00

The results show that the PNS and VSL wall pressures are in close agreement. The windward pressure values differ by less than 1%, while at the $\phi = 90$ deg plane these differences are of the order of 5%. Larger differences are seen at the point of crossflow separation; however, the VSL predictions at this location may not be very accurate. The inviscid NOL3D predictions also show less than 1% difference in the windward wall-pressure predictions. In the crossflow separated region, however, these inviscid results show much lower values of wall pressure than the corresponding VSL as well as PNS results.

Figures 2 and 3 show the axial and crossflow distributions of wall heat-transfer rates. These results show that along the windward surface the VSL and PNS predictions of wall heat-transfer rates are within 10% of each other. Along the $\phi = 90$ deg plane these differences increase to 15%, and are of the order of 40% at the point of crossflow separational. The streamwise skin-friction predictions also show similar trends.

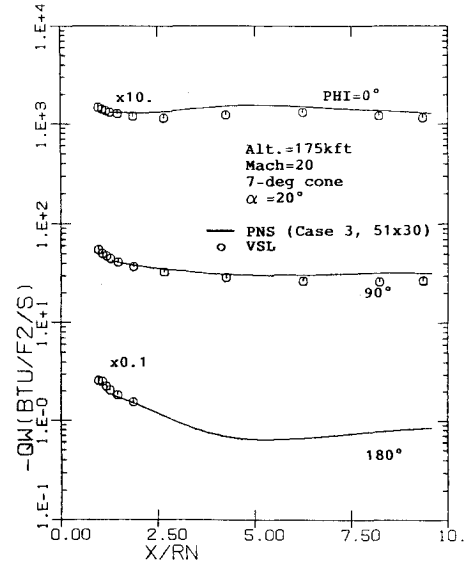

Fig. 2 Axial distribution of the wall heat-transfer rates.

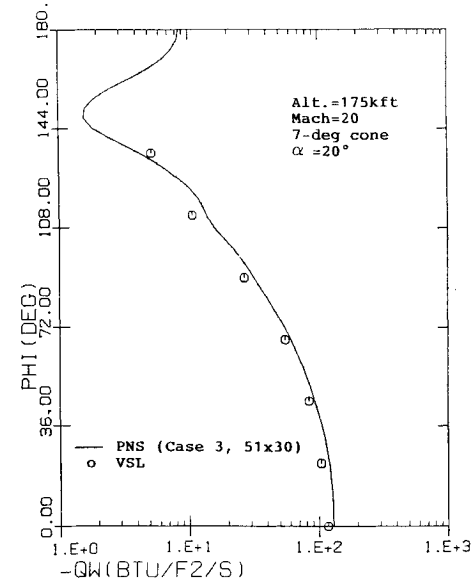

Fig. 3 Crossflow distribution of the wall heat-transfer rates at the body end.

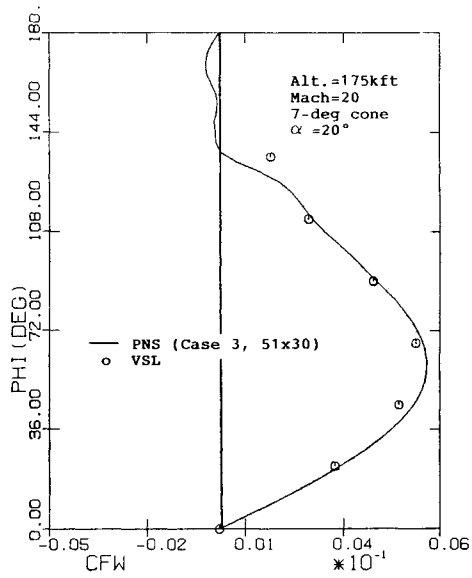

Fig. 4 Crossflow distribution of the crossflow skin-friction coefficient at the body end.

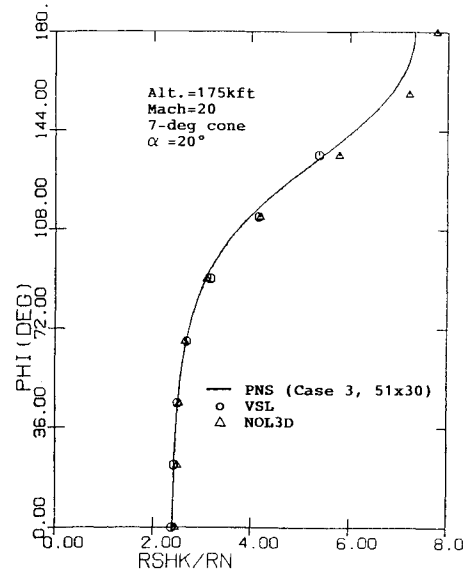

Fig. 6 Crossflow variation of the bow shock location at the body end.

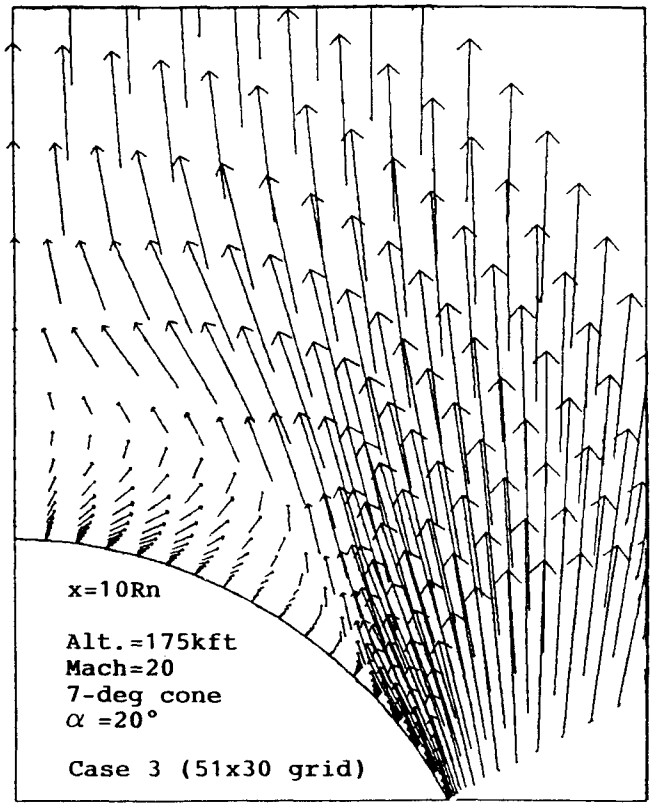

Fig. 5 Leeside crossflow velocity vector plot at the body end.

The circumferential distribution of the crossflow skin-friction coefficient at the body end is shown in Fig. 4. These results show that up until the point of crossflow separation, the VSL and PNS predictions are in good agreement with each other. The crossflow grid for the VSL solution is not fine enough to accurately predict the flowfield in the vicinity of the crossflow separation. However, the VSL solution does indicate that crossflow separation occurs somewhere between $\phi = 135$ and 157.5 deg. This is confirmed by the PNS calculations, which show the crossflow separation occuring around the $\phi = 140$ deg location (Fig. 5). The crossflow variation of the bow shock location at the body end is shown in Fig. 6. This figure shows that the inviscid NOL3D results overpredict the bow shock location on the leeward side by as much as 6%. The

Table 2 Comparison of force and moment data

Solution scheme		*CA*	*CN*	*−CM*	*XCP/L*
Parabolized Navier-Stokes	Case 1	0.3607	0.6106	0.3627	0.5941
	Case 2	0.3622	0.6163	0.3677	0.5951
	Case 3	0.3612	0.6161	0.3663	0.5945
Viscous shock-layer[a]		0.3544	0.5940	0.3554	0.5984
Inviscid		0.2763	0.5783	0.3412	0.5901

[a]These viscous shock-layer force and moment calculations assume that the surface pressure in the crossflow separated region can be approximated by the freestream pressure, and skin-friction in this crossflow separated region can be neglected.

VSL predictions, however, are in excellent agreement with the corresponding PNS predictions even up to the last circumferential grid point of the VSL solution ($\phi = 135$ deg).

The results of predicted force and moment coefficients at the body end are shown in Table 2. These results show that the VSL predictions of axial-force and the pitching-moment coefficients are within 2% of the corresponding PNS predictions. The normal-force coefficient differs by less than 3%, and the center-of-pressure location differs by only 0.7%. The VSL axial-force coefficient is smaller than the corresponding PNS predictions. This is understandable because these VSL force and moment calculations assume the surface pressure in the crossflow separated region to be the freestream pressure and, furthermore, neglect the skin-friction contribution in this region. In fact the PNS results show that the surface pressures in the crossflow separated region are typically of the order of 2-4 times the freestream pressure. This may account for some of the observed differences in the axial-force coefficients. The inviscid NOL3D results, on the other hand, underpredict the axial force by as much as 23%. But the normal force and pitching moments agree better and are within 6% of the corresponding PNS and VSL predictions. The inviscid center-of-pressure location is with 0.7% of the PNS predictions. For longer bodies, however, these differences between viscous and inviscid predictions of aerodynamic forces and moments may be more.

The crossflow variation of O concentration levels is shown in Fig. 7, which clearly shows the thick ionized layer on the leeside. The leeside pack O concentration levels are roughly three times larger than the windward side. The corresponding O_2 concentration levels are also consistent with the greater dissociation occurring on the leeside. The N_2 concentration levels follow the same trend as the O and O_2 concentration distributions; however, in this case the peak leeside concentra-

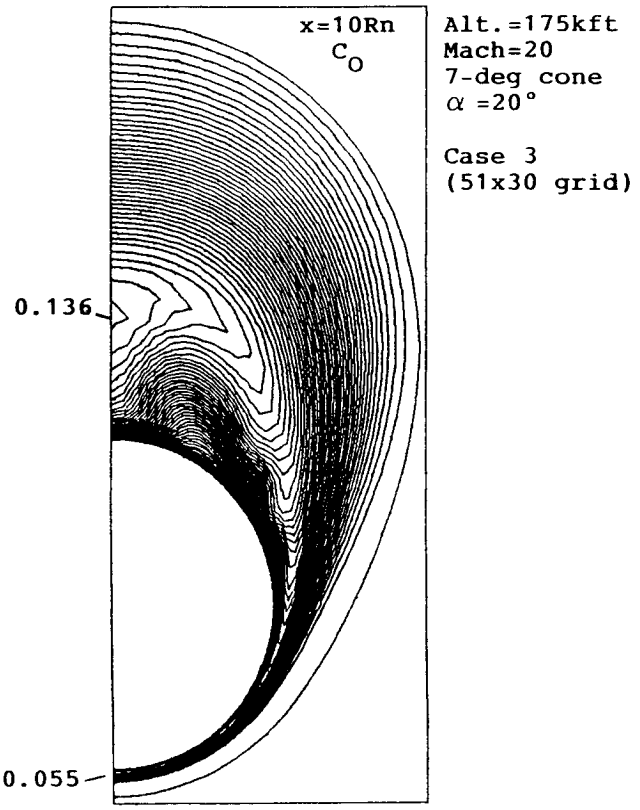

Fig. 7 Concentration contours of O at the body end.

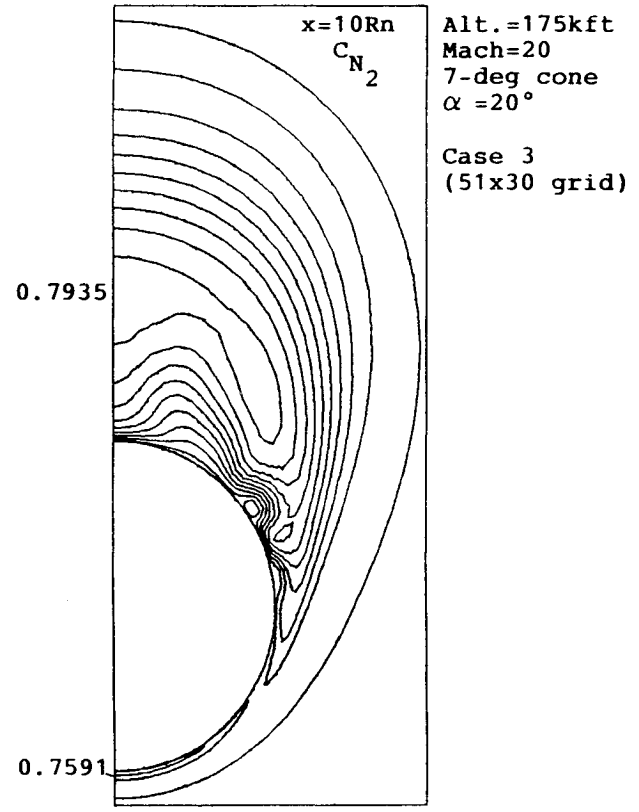

Fig. 8 Concentration contours of N_2 at the body end.

tions of N are roughly 40 times that of the windward side. Figure 8 shows the N_2 concentration contours and presents an interesting process not seen at low to moderate angles of attack (at least not to such a noticeable extent). The current results show that the N_2 concentration at the point of crossflow separation is larger than even the freestream. While this at first looks odd, it is understandable because first of all in the presence of viscous diffusion effects the local elemental mass fractions may not be the same as the freestream. Furthermore, under these large-angle-of-attack conditions there are very strong crossflow convection effects (see Fig. 5). Since N_2 is the dominant species, it is strongly convected toward the point of crossflow separation not only from the windward side but also from the leeside. This causes a local accumulation of the N_2 species in the vicinity of the crossflow separation.

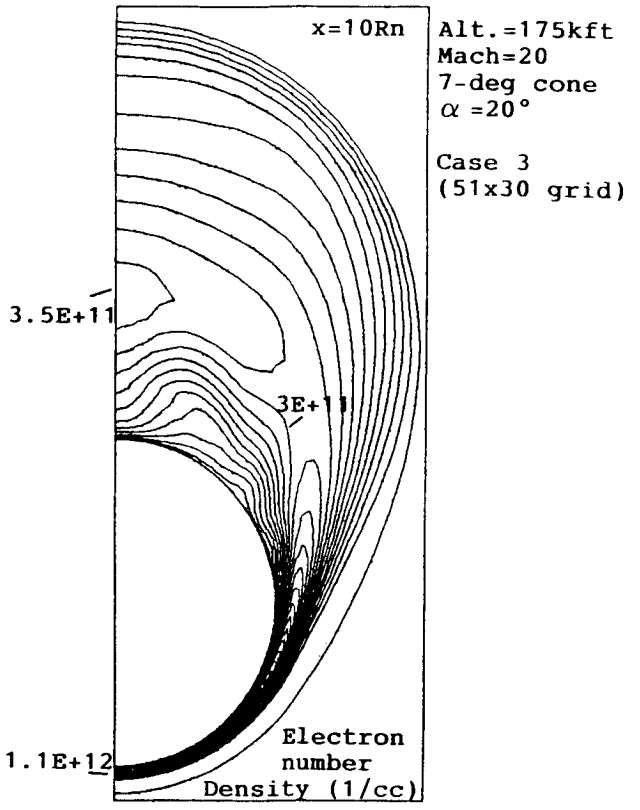

Fig. 9 Electron number density contours at the body end.

The NO and NO^+ concentration contours show that the peak NO concentration levels decrease as we move from the windward to the leeward side, whereas the peak NO^+ concentrations levels increase. The corresponding electron number-density contours are shown in Fig. 9. These results show that, for the case being considered, the peak ionization levels on the leeside are roughly six times greater than those on the windward side. Furthermore, the thickness of the ionized layer on the leeside is much greater than the windward side. It is quite obvious that the integrated contribution of the leeward side to the dissociated and ionized species feeding into the wake will be the most dominant. In other words, from a nonequilibrium chemistry point of view, an accurate modeling of the leeside chemistry and flowfield is very important. Furthermore, the existence of leeside crossflow separation does affect the leeside chemistry. Although an accurate modeling of the leeside flowfield and associated chemistry may not be very critical from the point of view of determining aerodynamic forces and moments, it is indeed very important from the point of view of the flowfield as well as wake chemistry.

In order to explore the grid refinement capabilities of the current three-dimensional nonequilibrium PNS scheme, we considered three different grid sizes. A comparison of cases 1 and 2 shows the effects of refining the grid in the axis-normal direction, while a comparison of cases 1 and 3 shows the effects of refining the grid in the crossflow direction. The results of these calculations show that the predicted wall pressures are relatively insensitive to grid refinement in either the axis-normal or the crossflow direction. The predicted wall

Table 3 Computing time

Case	x/Rn from-to	Grid $\xi_1 \times \xi_2 \times \xi_3$	IBM3090[a] $(m:s)$	XMP(4/8)[b] $(m:s)$	CRAY-2[c] $(m:s)$
Case 1	1.3 – 10.0	20×30×31	3:56	1:35	2:45
Case 2	1.3 – 10.0	20×50×31	5:46	2:20	4:00
Case 3	1.3 – 10.0	20×30×51	6:54	2:45	4:50

[a]Actual computing times on IBM 3090 with VS-compiler and scalar LEVEL = 3 optimization.
[b]Estimated computing times on X-MP (4/8) with CFT77 compiler and auto vectorization.
[c]Estimated computing times on CRAY-2 with CFT77 compiler and auto vectorization.

pressures with all three grids are within 1% of each other. The wall heat-transfer predictions show that in the crossflow-attached region ($x < 4Rn$), neither the additional axis-normal grid refinement nor the additional crossflow grid refinement had a significant impact on the predicted wall heat-transfer rates. In this region the predictions of the three grids used are within 5% of each other. In the crossflow-separated region ($x > 4Rn$) the axis-normal grid refinement changes the leeside wall heat-transfer rates by only 10% or less. The effect of crossflow grid refinement is, however, much more pronounced, and the results show that the use of a finer crossflow grid increases the predicted leeside wall heat-transfer rates by as much as 25%. This leads one to conclude that, under large angle-of-attack conditions, accurate modeling of the leeside flowfield and chemistry is more sensitive to the crossflow grid refinement than to the axis-normal grid refinement. The effects of grid refinement on the axial and crossflow distributions of the streamwise skin-friction coefficient follow the same trends as the corresponding wall heat-transfer predictions. These results also show that the grid refinement changes the force and moment coefficients by less than 1%, while the center-of-pressure location changes by less than 0.2%.

The computing time for the various calculations done in this study are shown in Table 3. When comparing the computing time for cases 1 and 2, we see that by increasing the axis-normal grid refinement the total number of grid points increase by a factor of 1.7; however, the corresponding computing times only increase by a factor of 1.5. This is because with the increased number of axis-normal grid points, the solution at each marching step converges at a faster rate and, thus, partially compensates the increase in overall computing times. As far as the effects of crossflow grid refinement on the computing times is concerned, since the solution scheme involves an implicit inversion algorithm in the crossflow direction, the computing times increase more rapidly than the corresponding increase in the crossflow grid refinement. Even so, the increase is not that much. For example, compared to case 1, case 3 has roughly 1.6 times more grid points, but the computing time for this case increases by a factor of only 1.75.

Conclusions

A new three-dimensional nonequilibrium PNS scheme has been developed to study three-dimensional hypersonic flows around multiconic configurations under large angle-of-attack conditions. This scheme is unconditionally time-like in the subsonic as well as the supersonic flow regions and does not require the use of any sublayer approximation. A new predictor-corrector solution scheme has been developed to treat the strong crossflow coupling effects in and around the crossflow separated regions. Furthermore, at the shock a new full implicit shock-prediction scheme has also been developed. This shock-fitting solution is fully coupled in the crossflow direction and shows very good stability and convergence characteristics.

The Mach 20 flowfield around a sphere-cone configuration at an angle of attack of 20 deg was predicted using three different computational grids to study the accuracy and efficiency of this new three-dimensional PNS scheme under large angle-of-attack conditions. The results of this study substantiate the following comments:

1) The current three-dimensional nonequilibrium results indicate that under large angle-of-attack conditions the leeward side has more dissociation of oxygen and nitrogen and formation of NO^+ than does the windward side. The dissociation is due to the much thicker high temperature region on the leeward side and, for other higher-velocity conditions, will undoubtedly result in a substantially increased electron density on the leeward side. If one is interested in the optical characteristics of the fluid on the leeward side, or if one is interested in the electron-density profiles for wake studies, this indicates that an accurate treatment of the leeward side will be essential.

2) The grid refinement studies show that the developed PNS scheme has very good grid-refinement characteristics. Furthermore, the results indicate that, in the crossflow separated region, sufficient crossflow and axis-normal grid refinement is essential to accurately capture the various crossflow details that have a significant impact on the local wall heat-transfer and skin-friction predictions.

3) These results also show that with the pseudo-unsteady algorithm used, the present fully iterative three-dimensional results can be obtained accurately and efficiently without any significant computing-time penalty. Furthermore, the enhanced solution accuracy allows for large marching steps to be used, and this substantially reduces the final computing times.

References

[1]Walberg, G. D., "A Survey of Aeroassisted Orbit Transfer," *Journal of Spacecraft and Rocket,* Vol. 22, Jan.-Feb. 1985, pp. 3-18.

[2]Blottner, F. G., Johnson, M., and Ellis, M., "Chemically Reacting Viscous Flow Program for Multi-Component Gas Mixtures," Sandia Laboratories, Albuquerque, NM, Report SC-RR-70-754, Dec. 1971.

[3]Miner, E. W. and Lewis, C. H., "Hypersonic Ionizing Air Viscous Shock-Layer Flows Over Nonanalytic Blunt Bodies," NASA CR-2550, May 1975.

[4]Kim, M. D., Swaminathan, S., and Lewis, C. H., "Three-Dimensional Nonequilibrium Viscous Shock-Layer Flow Over the Space Shuttle Orbiter," *Journal of Spacecraft and Rockets,* Vol. 21, Jan.-Feb. 1984, pp. 29-35; also, AIAA Paper 83-0487, Jan. 1983.

[5]Swaminathan, S., Kim, M. D., and Lewis, C. H., "Nonequilibrium Viscous Shock-Layer Flows Over Blunt Sphere-Cones at Angle of Attack," *Journal of Spacecraft and Rockets,* Vol. 20, July-Aug. 1983, pp. 331-338; also, AIAA Paper 82-0825, June 1982.

[6]Bhutta, B. A. and Lewis, C. H., "Low Reynolds Number Flows Past Complex Multiconic Geometries," AIAA Paper 85-0362, Jan. 1985.

[7]Bhutta, B. A. and Lewis, C. H., "An Implicit Parabolized Navier-Stokes Scheme for High-Altitude Reentry Flows," AIAA Paper 85-0036, Jan. 1985.

[8]Bhutta, B. A. and Lewis, C. H., "Prediction of Three-Dimensional Hypersonic Reentry Flows Using a PNS Scheme," AIAA Paper 85-1604, July 1985.

[9]Bhutta, B. A. and Lewis C. H., "Parabolized Navier-Stokes Predictions of High-Altitude Reentry Flowfields," VRA, Inc., Blacksburg, VA, VRA-TR-85-02, April 1985.

[10]Bhutta, B. A., Lewis, C. H., and Kautz II, F. A., "A Fast Fully Iterative Parabolized Navier-Stokes Scheme for Chemically Reacting Reentry Flows," AIAA Paper 85-0926, June 1985.

[11]Peyert, R. and Viviand, H., "Computations of Viscous Compressible Flows Based on the Navier-Stokes Equation," AGARD-AG-212, 1975.

[12]Viviand, H., "Conservative Forms of Gas Dynamics Equations," *La Recherche Aerospatiale,* No. 1, Jan.-Feb. 1974, pp. 65-68.

[13]Bird, R. B., Stewart, W. E., and Lightfoot, E. N., *Transport Phenomena,* Wiley, New York, 1960.

[14]Kaul, U.K. and Chaussee, D. S., "AFWAL Parabolized Navier-Stokes Coded: 1983 AFWAL/NASA Merged Baseline Version," Flight Dynamics Laboratory, Wright Aeronautical Laboratories, Wright-Patterson AFB, OH, AFWAL-TR-83-3118, Oct. 1983.

[15]Schiff, L. B. and Steger, J. L., "Numerical Simulation of Steady Supersonic Viscous Flows," AIAA Paper 79-0130, Jan. 1979.

[16]Shanks, S. P., Srinivasan, G. R., and Nicolet, W. E., "AFWAL Parabolized Navier-Stokes Code: Formulation and Users-Manual," Air Force Flight Dynamics Laboratory, Wright Patterson AFB, OH, AFWAL-TR-823034, June 1979.

[17]Browne, W. G., "Theromdynamic Properties of Some Atoms and

Atomic Ions," MSD Engineering Physics TM2, General Electric Co., Philadelphia, PA, 1962.

[18]Browne, W. G., "Thermodynamic Properties of Some Diatomic and Liner Polyatomic Molecules," MSD Engineering Physics TM3, General Electric Co., Philadelphia, PA, 1962.

[19]Browne, W. G., "Thermodynamic Properties of Some Diatomic and Diatomic Ions at High Temperatures," MSD Advanced Aerospace Physics TM8, General Electric Co., Philadelphia, PA, 1962.

[20]Bortner, M. H., "Chemical Kinetics in a Re-entry Flow Field," General Electric TIS R63SD63, Aug. 1963.

[21]Bhutta, B. A., Kautz II, F. A., and Lewis, C. H., "Influence of Aerodynamic Prediction Methodology on Performance Evaluation of Reentry Vehicle Configurations," *Journal of Spacecraft and Rockets*, Vol. 22, Sept.-Oct. 1985, pp. 541-547; also AIAA Paper 83-1799, July 1983.

[22]Thompson, R. A., Lewis, C. H., and Kautz, II, F. A., "Comparison Techniques for Predicting 3-D Viscous Flows Over Ablated Shapes," AIAA Paper 83-0345, Jan. 1983.

[23]Chaussee, D. S., Patterson, J. L., Kutler, P., Pulliam, T. H., and Steger, J. L., "A Numerical Simulation for Hypersonic Viscous Flows Over Arbitrary Geometries at High Angle of Attack," AIAA Paper 81-0050, Jan. 1981.

[24]Helliwell, W. S., Dickinson, R. P., and Lubard, S. C., "Viscous Flows Over Arbitrary Geometries at High Angle of Attack," AIAA Paper 80-0064, Jan. 1980.

[25]Lubard, S. C. and Helliwell, W. S., "Calculation of the Flow on a Cone at High Angle of Attack," R & D Associates, Santa Monica, CA, Report RDA-TR-150, Feb. 1973.

[26]Soloman, J. N., Ciment, M., Ferguson, R. E., Bell, J. B., and Wardlaw, Jr, A. B., "A Program for Computing Steady Inviscid Three-Dimensional Supersonic Flow on Reentry Vehicles, Vol. I., Analysis and Programming," Naval Surface Weapons Center, White Oak Laboratory, Silver Spring, MD, Report NSWC/WOL/Tr 77-28, Feb. 1977.